INTERNATIONAL JOURNAL FOR NUMERICAL METHODS IN FLUIDS
Int. J. Numer. Meth. Fluids 2005; **48**:467–499
Published online 14 February 2005 in Wiley InterScience (www.interscience.wiley.com). DOI: 10.1002/fld.934

Shear-thinning flow in weakly modulated channels

Ehab Abu-Ramadan and Roger E. Khayat*,†

Department of Mechanical and Materials Engineering, The University of Western Ontario, London, Ontario, Canada N6A 5B9

SUMMARY

The steady flow inside a spatially modulated channel is examined for shear-thinning and shear-thickening fluids. The flow is induced by the translation of the lower plate. The modulation amplitude is assumed to be small. A regular perturbation expansion of the flow field is used, coupled to a variable-step finite-difference scheme, to solve the problem. Convergence and accuracy assessment against finite-volume calculations indicates that there is a significant range of validity of the perturbation approach. The influence of the wall geometry, inertia and non-Newtonian effects are investigated systematically. In particular, the influence of the flow and fluid parameters is examined on the conditions for the onset of separation, vortex size and location. Copyright © 2005 John Wiley & Sons, Ltd.

KEY WORDS: spatially modulated channels; Couette flow; Carreau–Bird model; vortex formation

1. INTRODUCTION

This study examines the steady flow of a non-Newtonian fluid in a spatially modulated channel. The lower plate is assumed to be straight and moving at a constant velocity. The problem may be related to the viscous flow in a micro-channel with modulated walls, which is a classical problem that has attracted renewed interest because of its immediate relevance to novel micro-technologies, as in compact heat exchangers with high heat flux, and membrane blood oxygenators in extra-corporeal systems [1]. Other applications include the flow of polymeric fluids through porous media as encountered in tertiary oil recovery, in paper and textile coating, as well as in composite manufacturing processes [2]. Since flow in complex geometries, such as in modulated channels and tubes, can represent simple pore geometrical models, several experiments, and numerical studies using different models and solution techniques, exist for the prediction of non-Newtonian flow through complex geometries. In spite of the appar-

*Correspondence to: Roger E. Khayat, Department of Mechanical and Materials Engineering, The University of Western Ontario, London, Ontario, Canada N6A 5B9.
†E-mail: rkhayat@eng.uwo.ca

Contract/grant sponsor: Natural Sciences and Engineering Research Council of Canada

Received 12 August 2002
Revised 27 May 2004
Accepted 4 November 2004

ent geometrical simplicity, these flows can contain separated flow regions and exhibit many of the features present in much more complex geometries, which can significantly impact heat or mass transfer performance. This richness in physical phenomena in a relatively simple geometry is behind the ongoing fundamental interest. Moreover, this flow configuration provides an ideal setting for developing and testing the accuracy and efficiency of solution procedures.

For Newtonian fluids, Stephanoff *et al.* [3] were among the first to experimentally investigate the two-dimensional steady, unsteady and oscillatory flows in a furrowed channel at low Reynolds numbers for a modelled Oxford membrane blood oxygenator. Their work provided some qualitative support for the numerical model proposed by Sobey [1], based on a streamline-vorticity formulation. A further contribution to the flow characteristics in modulated channels was given by Nishimura *et al.* [4], who performed measurements in the Reynolds number range 40–10 000 to observe the steady flow characteristics in a channel with symmetric wavy walls, and provided an empirical relationship between wall shear stress and flow Reynolds number. Later, Nishimura *et al.* [5] performed another experimental investigation focusing on mass transfer from a channel with symmetric sinusoidal and arc-shaped walls. They investigated flow patterns and mass transfer characteristics in symmetrical two-dimensional sinusoidal and arc-shaped wavy-walled channels for Reynolds numbers, $Re \in [20–300]$. They observed that the arc-shaped channel faces an earlier transition to turbulence due to the formation of a new flow structure consisting of a regular three-dimensional flow at a low Reynolds number. In addition, mass transfer rate is enhanced in the case of the arc-shaped wall because of an earlier transition of turbulence when compared to the sinusoidal wall. Theoretical studies exist for the prediction of low-Reynolds-number flow in wavy channels. These can be broadly categorized as those dealing with heat/mass transfer characteristics, which necessarily focus on a narrow range of geometrical parameters [5–8], or on hydrodynamic simulations [1, 3, 4, 9–13]. These studies have focussed on the steady-state behaviour. Of the latter, much effort has been dedicated to developing solution techniques or suitable formulations for the problem. The techniques either consist of solving the Navier–Stokes equations or solving a perturbation problem either in terms of primitive or streamline-vorticity variables. The advantage of the perturbation approach is that it can be much faster than a full simulation, but due to the truncation error inherent in the method is subject to larger uncertainties. There is, however, little literature dedicated to the quantification of the accuracy or comparison of different techniques.

Existing theoretical studies may be divided into three categories, depending on the formulation of the physical domain. In a first approach, the modulated flow domain is mapped onto a rectangular computational domain to simplify the boundary conditions and to facilitate the integration process [14]. Benjamin [9] considered a co-ordinate system based on streamlines of inviscid flow over a wavy wall in his analysis of shear flow over wavy walls. Sobey [1] analysed the flow through furrowed channels and used an analytical mapping resulting in a non-orthogonal co-ordinate system. Caponi *et al.* [15] employed an orthogonal transformation expressed in terms of an infinite Fourier series in their analysis of boundary layers over modulated surfaces. Tanda and Vittori [6] carried out the investigation of fluid flow and heat transfer in a two-dimensional wavy channel by using another non-orthogonal transformation [7]. They examined the effect of geometry, Reynolds and Prandtl numbers on the flow field and heat transfer characteristics for a two-dimensional wavy channel. It was found that while pressure drop of the wavy channel is always larger than that of the straight channel,

heat transfer performance decreases or increases depending on the value of the physical and geometrical parameters.

In a second approach, the problem is solved directly in the physical domain such that the governing equations retain a very simple form. However, one has to develop special procedures for the imposition of boundary conditions. The most popular procedure is following a perturbation method, which involves the transfer of boundary conditions to a certain mean location of the boundary, resulting in a regular computational domain [10]. The accuracy of this approach depends on the amplitude of the modulation and the type of boundary conditions transfer procedure. This method is of interest due to its simplicity and due to the fact that in many applications, the interest lies in small modulation where the perturbation method provides reasonable accuracy. The accuracy of the perturbation approach in handling non-linear partial differential equations is well established. The interested reader is referred to the books by Nayfeh [16, 17] or more recently by Shivamoggi [18] for a complete discussion on the validity of the perturbation approach. Vajravelu [8] applied this perturbation method, carrying out a numerical study of flow through weakly modulated wavy channels. The effect of wall waviness was examined on the flow and heat transfer characteristics of plane Poiseuille flow for symmetric and asymmetric channels. An accurate spectral approach has also been implemented by Deane *et al*. [19] to simulate the flow inside converging–diverging channels. Szumbarski and Floryan [20] also developed a direct spectral method for the determination of flows in modulated channels. They, however, treated the flow problem as an internal rather than a boundary-value problem, where the flow conditions were specified along a line in the interior of the computational domain. A third approach is the combination of the above two approaches. By taking advantage of the mapping approach, one also adopts the essence of the perturbation method to reduce the complicated transformed governing equations into a set of ordinary differential equations subject to simple boundary conditions. Tsangaris and Leiter [12] performed a study on laminar steady flow in sinusoidal channels, using a perturbation method. The position of the beginning separation on the channel walls and the associated critical Reynolds number were determined, as well as the extension of the region of the separated flow. Above the critical Reynolds number, the position of separation and reattachment points were obtained as function of Reynolds number. Selvarajan *et al*. [13] also employed this method to investigate the flow through wavy-walled channels. As stated before, the accuracy of this approach depends on the amplitude of the modulation. In their study, the channel walls describe a travelling wave motion, where the boundary conditions are applied at the mean surface of the channel and the first-order perturbation quantities are calculated using the pseudospectral collocation method. Although this method is limited by the linear analysis, it is not restricted by any geometrical or physical parameters. In addition to the introduction of the numerical method this study presented the geometrical effects on the variations in velocity and pressure. Based on the computed wall shear stresses, the positions of flow separation and reattachment were also determined.

It is worth mentioning some of the studies conducted on unsteady flow. The unsteady non-isothermal flow was considered by Wang and Vanka [21]. Comparison of their numerical results on the rates of heat transfer for flow through a periodic array of wavy passages with those of a parallel-plate channel showed that although the average Nusselt numbers for the wavy wall channel are only slightly larger than those for a parallel-plate channel, the enhancement of heat transfer is about a factor of 2.5 in the transitional-flow regime. In addition, while the friction factors for the wavy channel were about twice those for the parallel-plate channel

in the steady-flow region, it remained almost constant in the transitional regime. It should be mentioned that those results explain the reason behind which corrugated channels enhance heat and mass transfer coefficients as suggested earlier by Sobey *et al.* [1, 3]. Selvarajan *et al.* [11] studied numerically the linear temporal stability characteristics of converging–diverging, symmetric wavy-walled channel flows. The disturbance equations are derived within the framework of Floquet theory and solved using the spectral collocation method. It was found that two-dimensional stability calculations indicate the presence of fast growing unstable modes that arise due to the waviness of the walls. Guzman and Amon [22, 23] investigated the transition process from laminar to chaotic flow in converging–diverging channels. They carried out a direct three-dimensional numerical simulation in a fully developed periodic regime for a uniform heat flux density at the bottom wall; the top wall was assumed to be adiabatic. Beyond a critical Reynolds number, they proved the existence of an unsteady periodic behaviour with higher harmonics. As the Reynolds number is increased further, a quasi-periodic behaviour is observed, with two incommensurable frequencies (torus T2). The flow eventually exhibits chaotic behaviour. The onset of unsteady motion is in accord with the linear stability analysis of Blancher *et al.* [24].

The flow of non-Newtonian fluids in modulated structures has also been studied, but to a much lesser extent. Ahrens *et al.* [25] used the undulating tube geometry and a first-order domain perturbation analysis to investigate the change of type occurring in the vorticity equation from elliptic to hyperbolic at high Reynolds number. However, this study failed to predict any changes to the flow resistance resulting from the modulation. Using a similar geometry, Pilitsis and Beris [2] improved Ahrens analysis by introducing a second-order perturbation analysis for an upper convected Maxwell fluid (UCM), which agrees with the flow resistance results obtained through the pseudospectral finite difference method (PSFD). In addition, a modification for the PSFD method was used [2] for an Oldroyd-B fluid. The modification was implemented in a stretched cylindrical system. However, none of these studies predicted a substantial increase in the flow resistance with increasing flow elasticity, for both fluid models. This result disagrees with the experimental results obtained by Marshal and Metzner [26], which show that one of the principle effects caused by the presence of viscoelasticity is a substantially higher flow resistance. In order to explain the deviation of the calculated results from the experiment, Beris *et al.* [27] used the Geisekus model [28], which has the advantage of incorporating an additional parameter that can predict a non-zero second normal stress coefficient. In addition, the model can predict a shear-thinning behaviour. Although Beris *et al.* used a corrugated channel instead of the corrugated tube (allowing the use of a finer mesh), the obtained results could not predict the deviation from the experimental results either, and led to the conclusion that the flow resistance might be due to a mechanism other than the constitutive model used. In addition, calculations with the Geiskus model exhibit numerical difficulties for small and large Weissenberg number (We). More importantly, the formulation of Beris *et al.* [27] did not predict any vortex formation. Vortex evolution was predicted by Pilitsis and Beris [29], who used a mixed pseudospectral finite difference technique in the simulation of steady state Oldroyd-B flow through corrugated tube. Viscoelasticity affects the shape and the size of the vortex, but was predicted only for large amplitude modulation and creeping flow.

In an effort to understand the departure of polymeric flow from Newtonian behaviour, Davidson *et al.* [30] constructed an apparatus that can provide information for testing constitutive equations for polymeric liquids in complex flows. This apparatus applies laser Doppler

velocimetry and flow birefringence to non-intrusive measurement of local velocity and stress fields in complex two-dimensional flows. This apparatus was used to investigate the flow behaviour of 20% polystyrene solution in a periodically constricted channel [31]. The results were compared with theory for the Newtonian, generalized Newtonian, upper convected Maxwell, and White Metzner models. The departures from Newtonian behaviour were explored through the velocity and stress fields. Comparison between theory and experiment showed that although all of the models predict a similar qualitative picture for the velocity and stress fields, none of them can predict the stress fields at any Weissenberg number. Pilitsis *et al.* [32] examined theoretically the combined effects of inertia and viscoelasticity for different constitutive models. Although separation was predicted, there was little emphasis on the influence of non-Newtonian effects on the conditions for onset of backflow. Other constitutive models have also been used for the flow between two rigid boundaries [33].

The present paper aims to correct two apparent deficiencies gleaned from the above literature review. First, there has not been any systematic study on the interplay between inertia and non-Newtonian effects. The present study emphasizes, particularly, the influence of inertia and non-Newtonian effects on the conditions for the onset of backflow, vortex size and location. In addition, although the perturbation approach has been widely used, there has not been a systematic assessment of the uncertainty of this approach. Thus, part of the paper is devoted to error assessment. Moreover, the influence of the channel modulation amplitude and wavelength as well as the non-Newtonian fluid parameters, on the critical Reynolds number for the appearance of flow reversal has been studied previously only over very small ranges. Results for Newtonian flow will be revisited, with comparison made against results obtained from a traditional finite-volume formulation. Extensive comparative study that established the range of validity of the perturbation approach proposed here was carried out recently by Zhou *et al.* [34]. The hydrodynamic features of steady flow in modulated channels will be described in a systematic and coherent way.

2. PROBLEM FORMULATION AND SOLUTION PROCEDURE

In this section, the general equations and boundary conditions for the Couette flow with spatially modulated walls are derived for small-amplitude modulation. The examined fluid viscosity is governed by the Carreau viscosity equation. A regular perturbation expansion for the flow field is carried out after the equations are mapped over a rectangular domain, reducing the problem to a set of ordinary differential equations, which will be solved using a variable-step-finite-difference scheme.

2.1. Governing equations

Consider the steady-state flow of an incompressible non-Newtonian fluid of density ρ. The viscosity, μ^*, is assumed to obey the Carreau–Bird model [35]

$$\frac{\mu^* - \mu_\infty}{\mu_0 - \mu_\infty} = [1 + (\Lambda\dot{\Gamma})^2]^{(n-1)/2} \tag{1}$$

where μ_0 is the zero-shear-rate viscosity, μ_∞ the infinite-shear-rate viscosity, Λ a time constant and n the power-law index. If n is less than 1, the fluid exhibits shear-thinning behaviour. If n is larger than 1, the fluid becomes shear thickening. In addition, this model predicts Newtonian fluid behaviour when $n=1$, $\Lambda=0$ or both. In other words, this model represents a Newtonian fluid when $\mu=\mu_0$. Here, $\dot{\Gamma}$ is the magnitude of rate-of-strain tensor, $\dot{\Gamma}_{ij}$

$$\dot{\Gamma}=\sqrt{\tfrac{1}{2}\dot{\Gamma}_{ij}\dot{\Gamma}_{ji}}, \quad \dot{\Gamma}_{ij}=U_{i,j}+U_{j,i} \tag{2}$$

where U_i is the velocity component in the ith direction, and a comma denotes partial differentiation. The fluid is assumed to lie between two infinite rigid boundaries, the lower wall being straight and moving at a constant velocity U_w, while the upper boundary being periodically modulated and at rest. The problem is first introduced in the (X,Y) plane, with the X-axis coinciding with the lower wall. The general shapes of the lower and upper boundaries are thus given by $Y=0$ and $Y=D+Af(X)$, respectively, where A is the modulation amplitude, and D the mean gap width. Here $f(X)$ is a general function of X that may be arbitrarily prescribed. In this work, however, only a sinusoidal modulation will be considered.

The general conservation of mass and linear momentum equations are given by

$$\nabla\cdot\mathbf{U}=0 \tag{3a}$$

$$\rho\mathbf{U}\cdot\nabla\mathbf{U}=\nabla\cdot\lfloor\mu^*(\nabla\mathbf{U}+\nabla\mathbf{U}^{\mathrm{t}})\rfloor-\nabla P \tag{3b}$$

where $\mathbf{U}(U,V)$ is the velocity vector, P the pressure, ∇ the gradient operator, and t donates transpose. The fluid is assumed to adhere to the rigid boundaries, and the no-slip and no-penetration boundary conditions are written as

$$U(X,Y=0)=U_w, \quad V(X,Y=0)=0 \tag{4a}$$

$$U(X,Y=D+Af(X))=V(X,Y=D+Af(x))=0 \tag{4b}$$

It is convenient to cast the problem in terms of dimensionless terms, which are introduced as follows:

$$\begin{aligned} x&=\frac{X}{D}, \qquad y=\frac{Y}{D}, \qquad u=\frac{U}{U_w}\\ v&=\frac{V}{U_w}, \quad p=\frac{DP}{\mu_0 U_w}, \quad \mu=\frac{\mu^*}{\mu_0}\end{aligned} \tag{5}$$

where x and y are the co-ordinates, u and v are the velocity components, p is the pressure, and μ is the viscosity, in dimensionless form. There are four important dimensionless groups emerging in the problem, namely, the Reynolds number Re, Deborah number De, viscosity ratio s, and the aspect ratio ε

$$Re=\frac{\rho U_w D}{\mu_0}, \quad De=\frac{\Lambda U_w}{D}, \quad s=\frac{\mu_\infty}{\mu_0}, \quad \varepsilon=\frac{A}{D} \tag{6}$$

The expression for the viscosity becomes

$$\mu = s + (1-s)[1 + De^2\dot{\gamma}^2]^{(n-1)/2}; \quad \dot{\gamma} = \sqrt{2u_x^2 + u_y^2 + 2u_y v_x + v_x^2 + 2v_y^2} \tag{7}$$

where, in the sequel, a subscript denotes partial differentiation. The governing equations may be rewritten as

$$u_x + v_y = 0 \tag{8a}$$

$$Re(uu_x + vu_y) = 2\mu_x u_x + \mu_y(u_y + v_x) + \mu(u_{xx} + u_{yy}) - p_x \tag{8b}$$

$$Re(uv_x + vv_y) = \mu_x(v_x + u_y) + 2\mu_y v_y + \mu(v_{xx} + v_{yy}) - p_y \tag{8c}$$

The above equations must be solved subject to the conditions

$$u(x, y=0) = 1, \quad v(x, y=0) = u(x, y=1+\varepsilon f(x)) = v(x, y=1+\varepsilon f(x)) = 0 \tag{9a}$$

and spatial periodicity

$$\begin{aligned} &u(x=0, y) = u\left(x=\frac{2\pi}{\alpha}, y\right), \quad v(x=0, y) = v\left(x=\frac{2\pi}{\alpha}, y\right) \\ &p(x=0, y) = p\left(x=\frac{2\pi}{\alpha}, y\right) \end{aligned} \tag{9b}$$

where α is the dimensionless wavenumber of the wall modulation. The periodicity of the pressure field results from the periodic nature of the flow. Numerical investigation using the finite-element method showed that the pressure field is periodic with a periodicity equal to the geometric modulation periodicity (see [36, Figures 14 and 15]). Unlike pressure-driven flow problems, the term accounting for linear pressure drop is equal to zero for the current problem. The periodicity of the pressure field will be further discussed when numerical assessment is introduced in Section 3.5. Problems (7)–(9) are defined over the physical domain $\Omega_{xy} = \{(x, y) | x \in [0, 2\pi/\alpha], y \in [0, 1 + \varepsilon f(x)]\}$, as depicted, schematically, from Figure 1. This domain is next mapped onto the rectangular domain.

2.2. Domain transformation

The periodic physical domain Ω_{xy} is mapped onto the rectangular domain $\Omega_{\xi\eta} = \{(\xi, \eta) | \xi \in [0, 2\pi/\alpha], \eta \in [0, 1]\}$. In this case,

$$\xi(x, y) = x, \quad \eta(x, y) = \frac{y}{h(x)} \tag{10}$$

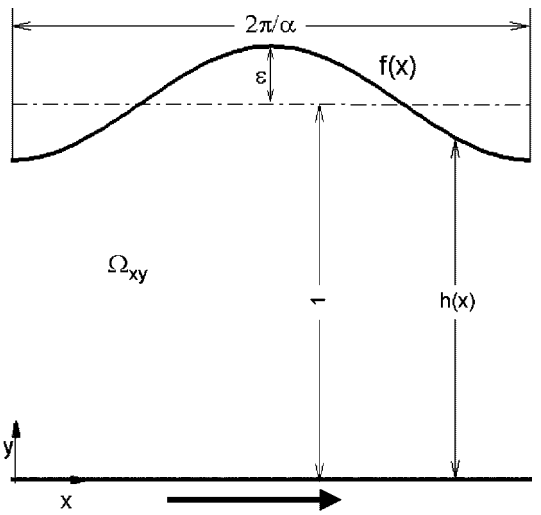

Figure 1. Physical domain and flow configuration for spatially modulated channel (dimensionless notation is used).

where $h(x)=1+\varepsilon f(x)$ is the dimensionless gap. Now the transformed equations read

$$u_\xi - \frac{\eta h'}{h}u_\eta + \frac{1}{h}v_\eta = 0 \tag{11a}$$

$$\begin{aligned} &Re\left[u\left(u_\xi - \frac{\eta h'}{h}u_\eta\right) + \frac{vu_\eta}{h}\right] \\ &\quad = -p_\xi + \frac{\eta h'}{h}p_\eta + 2\left(\mu_\xi - \frac{\eta h'}{h}\mu_\eta\right)\left(u_\xi - \frac{\eta h'}{h}u_\eta\right) + \frac{\mu_\eta u_\eta}{h^2}\left(\frac{u_\eta}{h} + v_\xi - v_\eta\frac{\eta h'}{h}\right) \\ &\quad +\mu\left\{u_{\xi\xi} + \frac{u_{\eta\eta}}{h^2} - \eta\left[\left(\frac{h''}{h} - \left(\frac{h'}{h}\right)^2\right)u_\eta + \frac{h'}{h}u_{\eta\xi}\right]\right. \\ &\quad \left. -\frac{\eta h'}{h}\left(u_{\xi\eta} - \frac{\eta h'}{h}u_{\eta\eta} - \frac{h'}{h}u_\eta\right)\right\} \end{aligned} \tag{11b}$$

$$\begin{aligned} &Re\left[u\left(v_\xi - \frac{\eta h'}{h}v_\eta\right) + \frac{vv_\eta}{h}\right] \\ &\quad = \frac{-p_\eta}{h} + \left(\mu_\xi - \frac{\eta h'}{h}\mu_\eta\right)\left(\frac{u_\eta}{h} + v_\xi - \frac{\eta h'}{h}v_\eta\right) + \frac{2\mu_\eta v_\eta}{h^2} \end{aligned}$$

$$+\mu\left\{\frac{v_{\eta\eta}}{h^2}+v_{\xi\xi}-\eta\left[\left(\frac{h''}{h}-\left(\frac{h'}{h}\right)^2\right)v_\eta+\frac{h'}{h}v_{\eta\xi}\right]\right.$$
$$\left.-\frac{\eta h'}{h}\left(v_{\xi\eta}-\frac{\eta h'}{h}v_{\eta\eta}-\frac{h'}{h}v_\eta\right)\right\} \tag{11c}$$

where a prime denotes total differentiation. The boundary conditions are

$$u(\xi,\eta=0)=1,\quad u(\xi,\eta=1)=v(\xi,\eta=0)=v(\xi,\eta=1)=0$$
$$u(\xi=0,\eta)=u\left(\xi=\frac{2\pi}{\alpha},\eta\right),\quad v(\xi=0,\eta)=v\left(\xi=\frac{2\pi}{\alpha},\eta\right) \tag{12}$$
$$p(\xi=0,\eta)=p\left(\xi=\frac{2\pi}{\alpha},\eta\right)$$

The solution of Problems (11)–(12) is sought next.

2.3. The perturbation solution

In this work, only small amplitude modulation is examined, so that ε is small ($\varepsilon \ll 1$). In this case, a regular perturbation expansion is used for the velocity and pressure. At this point, it is necessary to introduce explicitly the modulated wall profile, f. Various configurations may be easily incorporated in the general formulation above. For instance, both walls could be assumed to be modulated, and the modulation can be represented by a general Fourier series, as long as the wall profile is smooth. In this work, however, only the upper wall is assumed to be modulated in the form of a sine wave such that

$$f(\xi)=-\cos(\alpha\xi) \tag{13}$$

where α is recalled to be the (dimensionless) wavenumber. In this case, the general solution to problems (11)–(12) may be written as

$$u(\xi,\eta)=u_0(\xi,\eta)+\varepsilon[u_1(\eta)\sin(\alpha\xi)+u_2(\eta)\cos(\alpha\xi)]+O(\varepsilon^2)$$
$$v(\xi,\eta)=v_0(\xi,\eta)+\varepsilon[v_1(\eta)\sin(\alpha\xi)+v_2(\eta)\cos(\alpha\xi)]+O(\varepsilon^2) \tag{14}$$
$$p(\xi,\eta)=p_0(\xi,\eta)+\varepsilon[p_1(\eta)\sin(\alpha\xi)+p_2(\eta)\cos(\alpha\xi)]+O(\varepsilon^2)$$

where terms of $O(\varepsilon^2)$ and higher are neglected. Substitution of expressions (14) into Equations (11) and conditions (12), and expanding the viscosity expression, lead to a hierarchy of equations for the unknown coefficients u_i, v_i and $p_i (i=0,1,2)$, which must be solved to each order in ε. Thus, to leading order in ε, one recovers the equations encountered in basic Couette flow. Correspondingly, the solution is given by

$$u_0(\xi,\eta)=1-\eta,\quad v_0(\xi,\eta)=p_0(\xi,\eta)=0 \tag{15}$$

The equations for the higher-order terms read

$$v_{1\eta} = -\alpha\eta + \alpha u_2 \tag{16a}$$

$$v_{2\eta} = -\alpha u_1 \tag{16b}$$

$$\begin{aligned} p_{1\eta} = Re\alpha v_2(1-\eta) + (v_{1\eta\eta} - v_1\alpha^2)[s + (1-s)(1+De^2)^{(n-1)/2}] \\ -\alpha De^2(n-1)(1-s)(1+De^2)^{(n-3)/2}(u_{2\eta} + \alpha v_1 - 1) \end{aligned} \tag{16c}$$

$$\begin{aligned} p_{2\eta} = -Re\alpha v_1(1-\eta) + (v_{2\eta\eta} - v_2\alpha^2)[s + (1-s)(1+De^2)^{(n-1)/2}] \\ +\alpha De^2(n-1)(1-s)(1+De^2)^{(n-3)/2}(u_{1\eta} - \alpha v_2) \end{aligned} \tag{16d}$$

$$\begin{aligned} -u_{1\eta\eta}\{(1-s)(1+De^2)^{(n-3)/2}(1+nDe^2) + s\} \\ = -Re(-u_2\alpha(1-\eta) + \eta\alpha(1-\eta) - v_1) \\ + p_2\alpha - v_{2\eta}\alpha De^2(n-1)(1-s)(1+De^2)^{(n-3)/2} \\ - u_1\alpha^2[(1-s)(1+De^2)^{(n-1)/2} + s] \end{aligned} \tag{16e}$$

$$\begin{aligned} -u_{2\eta\eta}\{(1-s)(1+De^2)^{(n-3)/2}(1+nDe^2) + s\} \\ = -Re(u_1\alpha(1-\eta) - v_2) \\ - p_1\alpha + v_{1\eta}\alpha De^2(n-1)(1-s)(1+De^2)^{(n-3)/2} \\ + \alpha^2(\eta - u_2)[(1-s)(1+De^2)^{(n-1)/2} + s] \end{aligned} \tag{16f}$$

The system above is a set of non-homogenous ordinary differential equations, which together with the corresponding homogeneous boundary conditions

$$u_1 = u_2 = v_1 = v_2 = 0 \quad \text{at } \eta = 0 \text{ and } \eta = 1 \tag{17}$$

constitute a boundary-value problem of the two-point type. A variable-step finite-difference scheme is used to obtain the solution [37]. The basic discretization is the trapezoidal rule over a non-uniform mesh. This mesh is chosen adaptively, to make the local error approximately the same size everywhere. Higher-order discretizations are obtained by differed corrections and global error estimates are produced to control the computation. The linear system of equations is solved using a special form of Gauss elimination that preserves sparseness.

3. DISCUSSION AND RESULTS

In this section, the flow inside a weakly modulated channel will be considered for both Newtonian and non-Newtonian flows. Numerical accuracy and convergence will be assessed. A review of the literature shows that the range of validity of the perturbation method, for non-Newtonian flow, to predict flows in weakly modulated channels has not been rigorously established. Since this method is intended to provide a fast and accurate alternative to conventional methods in the limit of small modulation amplitude, establishing the accuracy of the solution is critical. In this section, a detailed study of the influence of geometric and flow parameters on solution accuracy, as well as a comparison to finite-volume predictions is provided. The results focus on the influence of inertia and non-Newtonian effects on the flow, for given modulation. In particular, the conditions for the onset of separation are closely examined for both shear-thinning and shear-thickening fluids.

3.1. General flow and assessment

Consider first the influence of the modulation amplitude on the flow rate, Q. Figure 2 displays the dependence of Q on the streamwise position. In general, mass is only approximately conserved, and the volume flow rate, $Q(x)$, varies (locally) with x, since the continuity equation is not exactly satisfied. This variation is generally in phase with the wall modulation, and increases with modulation amplitude, ε. The flow rate that is averaged over a modulation wavelength, Q_{ave}, is then considered as the exact value for Q. The maximum error occurs at the crests and troughs of the modulation wave of the wall, and is zero at the inflection points ($x = \lambda/4$ and $3\lambda/4$), which is expected since the truncated terms are multiplied by the sinusoidal waveform. The global relative error at a given streamwise location may then be

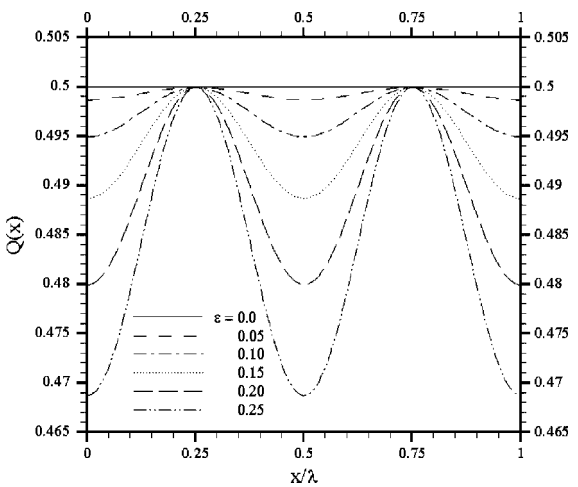

Figure 2. Streamwise variation of the predicted volume flow rate, Q, for $\varepsilon \in [0, 0.25]$. Note that the same curves are obtained essentially for any values of the remaining parameters.

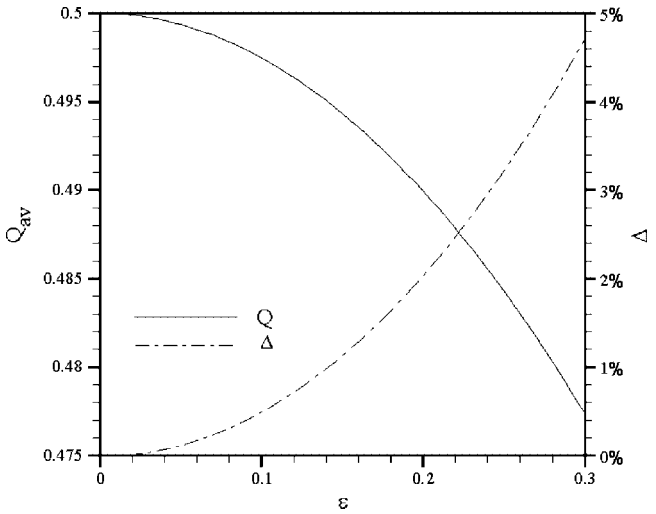

Figure 3. Average flow rate, and maximum relative error for mass conservation as functions of the modulation amplitude, ε. Note that the curves are essentially independent of the remaining parameters.

defined as

$$\Delta = \frac{|Q - Q_{\text{ave}}|_{\max}}{Q_{\text{ave}}} \tag{18}$$

Figure 3 displays the dependence of the average flow rate, and relative error, on ε, for the range $\varepsilon \in [0, 0.3]$. It is generally found that the flow rate decreases with ε, slowly at small ε. The influence of the modulation amplitude on the maximum error is reflected through the dependence of Δ on ε. As expected, the error is on the order of ε^2, and conservation of mass is generally satisfied to within 1% for $\varepsilon < 0.15$.

Extensive additional calculations were carried out, which show that the curves in Figures 2 and 3 are universal; that is, they essentially do not depend on the Reynolds number, Re, the modulation wavenumber, α, or whether the fluid is Newtonian or not. The only influencing parameter appears to be the modulation amplitude, ε. Error sources originate in the truncated terms of the governing equations. These terms contain combinations of the velocity gradients multiplied by coefficients containing the parameters α, ε and Re. Assuming that the (dimensionless) velocity gradients are of order 1, the error in the perturbation method should scale with the higher-order coefficients of order ε^2 and $\alpha\varepsilon^2$. The influence of the truncated terms in the continuity equation is conveniently summarized through the global error in mass conservation. Additional numerical assessment will be discussed later when comparison with CFD calculations is carried out.

The general flow response for a non-Newtonian fluid is typically illustrated in Figure 4 for a flow inside a channel with $\varepsilon = 0.15$, $\alpha = 1$ and $Re = 25$. Also, the fluid is shear thinning with $n = 0.6$, $De = 3$ and $s = 0$. The figure shows the streamlines, pressure, contours of the velocity components in the streamwise and depthwise directions, shear-rate magnitude and viscosity. Aside from the slight break in symmetry, the situation is very similar to that exhibited by creeping flow ($Re = 0$). Although the streamlines follow generally the channel wall profiles,

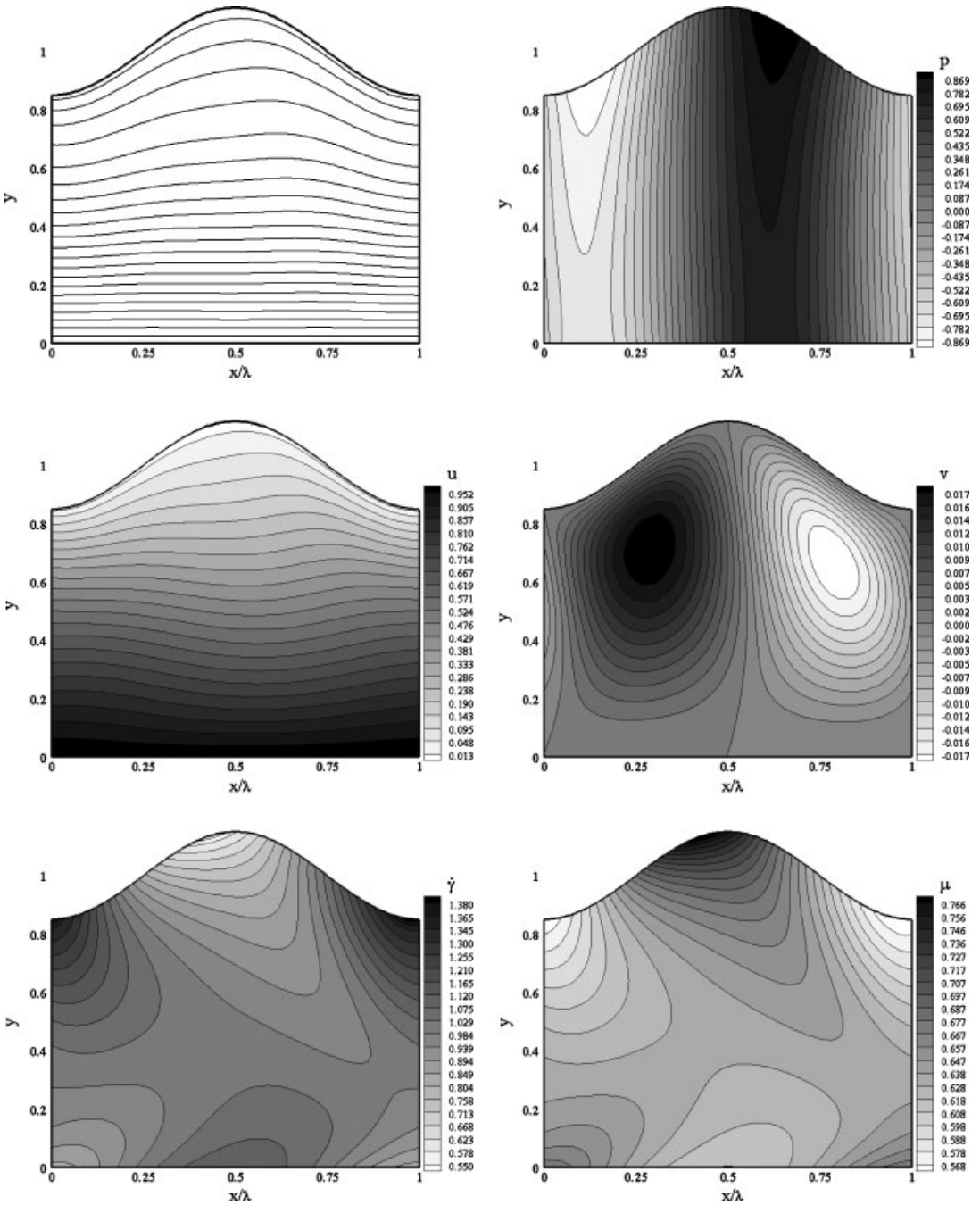

Figure 4. Typical response of a shear-thinning flow with low inertia ($Re = 25$). The figure displays the streamlines, the pressure, the contours of the streamwise and depthwise velocity components, shear-rate magnitude, and viscosity. Here $\varepsilon = 0.15$, $\alpha = 1$, $n = 0.6$, $De = 3$ and $s = 0$.

they exhibit a break in symmetry, which is due to the non-zero convective term uu_x in Equations (8). Note that since the viscosity is positive, non-Newtonian effects do not contribute to the break in symmetry, a fact that is easily verified from Equations (8). The pressure is essentially constant across the channel, except downstream of the crest and trough locations, where the pressure is maximum and minimum, respectively. For a given height, the maximum streamwise velocity occurs below the trough, which is expected based on continuity arguments alone given that the flow does not separate. The break in symmetry (or antisymmetry) is also reflected in the velocity contours. Inspection of the u and v contours shows that the depthwise flow is much weaker than the streamwise flow, on the order of less than 2%. It is also inferred that the changes in v with respect to both x and y are smaller than the change in u with respect to y. Moreover, u is not expected, given the weak modulation amplitude, to change rapidly with x. In fact, the flow behaves essentially like a thin film, except downstream below the crest and trough. Hence, further understanding of the flow is gained upon inspecting the solution based on the lubrication assumption, which in the absence of inertia, leads to the following expressions for the velocity and pressure gradient:

$$u(x,y)=\left(\frac{y}{h}-1\right)\left[\frac{3y}{h^2}(h-1)-1\right] \quad p_x(x)=\frac{6}{h^3}(h-1) \tag{19}$$

The expression for u confirms the results in Figure 4 (refer to u contours), and shows, in particular, that $u_x(x,y)=0$ whenever $h'=0$, and u reaches a maximum (minimum) along x whenever h reaches a minimum (maximum). The lubrication solution also predicts that the flow is linear with y when $h=1$ (at the inflection points).

The lubrication result gives some indication as to the strength of shear rate and, therefore, viscosity. The break in symmetry is more pronounced for the shear rate and viscosity contours. As expected, the viscosity is essentially a mirror image of the shear rate magnitude. The shear rate is observed to be maximum just below the trough and at the lower plate at $x=\lambda/2$, and is practically absent in the crest region. These observations are easily inferred from lubrication theory; since u_y is the dominant term, then the shear rate distribution may be estimated from expressions (19). Thus, the fluid behaves essentially as Newtonian in the crest region. There seems to be little qualitative influence of non-Newtonian effects when the results in Figure 4 are compared with those for $n=1$, with the exception of the viscosity distribution. However, the quantitative picture depends strongly on the type of fluid used.

While the flow topology is little affected by non-Newtonian effects, the forces on the walls can vary significantly from fluid to fluid. This is typically illustrated in Figures 5 and 6 for $De=3$, $s=0$, $\varepsilon=0.15$, $\alpha=1$ and $Re=25$, where, respectively, the normal and shear stresses, τ_n and τ_s, at the upper and lower walls are plotted against x/λ for $n\in[0.4,1.6]$. The normal stress curves are sinusoidal at both the upper and lower walls, and are essentially antisymmetric with respect to $x=\lambda/2$. Since elongational effects are weak, the normal stress is dominated by the pressure. Indeed, the curves corresponding to $n=0.6$ in Figure 5 indicate the same level of pressure as that reported in Figure 4. However, the normal stress level increases significantly with n. This shows that shear-thickening fluids are effective lubricants. The extrema are shifted downstream as n increases, as indicated by the loci of the extrema in Figure 5. The qualitative and quantitative similarity between the normal forces at the two walls is almost but not entirely inferable from the pressure contours in Figure 4. However, one can still infer from both Figures 4 and 5 that the normal stress (pressure) experiences

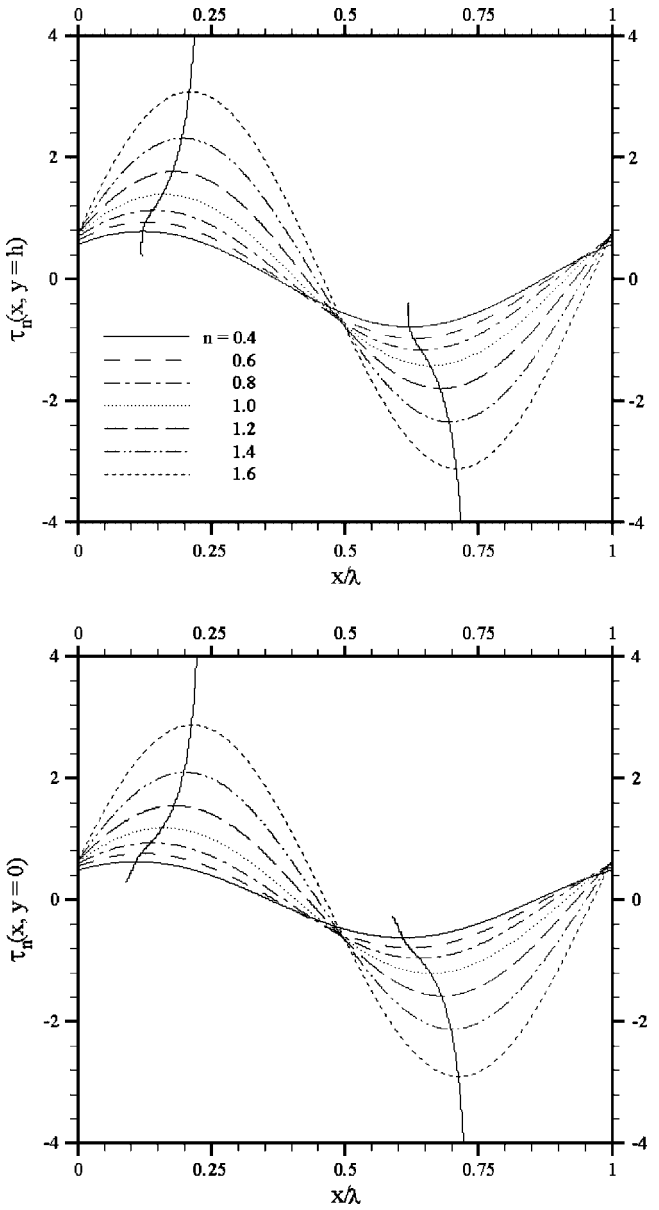

Figure 5. Influence of n (power law index) on the normal stress distribution at the upper (modulated) and lower (straight) walls for low inertia flow ($Re = 25$). Here $\varepsilon = 0.15$, $\alpha = 1$, $De = 3$ and $s = 0$.

a steeper change near the extrema at the upper than at the lower wall. In other words, the extrema occur at the same x locations at the two walls, but the normal force is slightly stronger at the upper wall. This observation is verified upon extensive comparison with the results obtained using the finite-volume method.

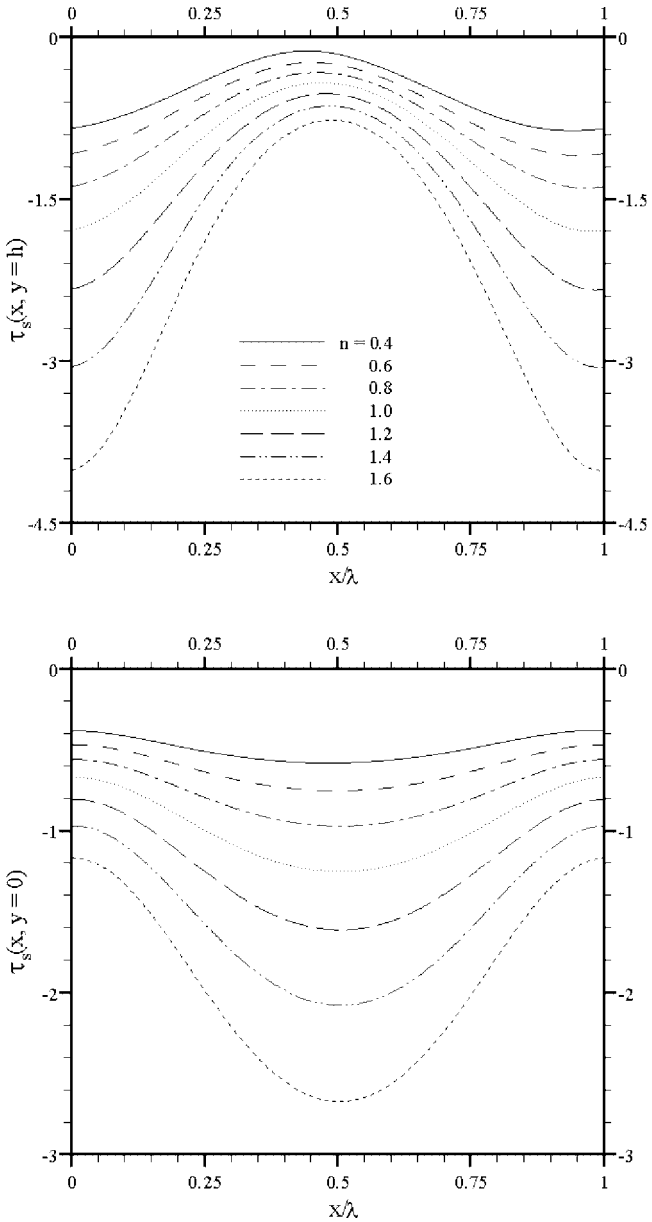

Figure 6. Influence of n (power law index) on the shear stress distribution at the upper (modulated) and lower (straight) walls for low inertia flow ($Re = 25$). Here $\varepsilon = 0.15$, $\alpha = 1$, $De = 3$ and $s = 0$.

In contrast, the shear stress distributions at the two walls tend to be dissimilar, as shown in Figure 6. The shear stress exhibits a maximum near $x = \lambda/2$ at the upper wall, the amplitude of which decreases as n increases. The minimum at the lower wall decreases significantly with n. There is almost symmetry with respect to $x = \lambda/2$ in τ_s at the lower wall only.

The break in τ_s symmetry with respect to $x = \lambda/2$ along the upper wall is more noticeable for shear thinning fluids. The shear stress distributions in Figure 6 are closely correlated with the (u) velocity contours in Figure 4. The large stress levels below the trough at the upper wall and below the crest at the lower wall reflect the sharp shearing effect depicted in Figure 4, and predicted by expression (19). The weak maximum near the crest at the upper wall reflects the weak streamwise flow, and hints at the region where separation is likely to occur (see next).

3.2. Interplay between inertia and non-Newtonian effects, and separation

It is well established, for Newtonian flow, that as the Reynolds number exceeds a certain threshold, flow separation occurs in the region of expansion (below the crest). In this case, the threshold depends on the modulation amplitude and wavelength. A similar response is expected for a non-Newtonian fluid, but shear thinning and thickening are expected to strongly influence the conditions for the onset of separation. It is helpful to first examine the overall influence of non-Newtonian effect on flow separation. Figure 7 illustrates typically the streamlines, pressure, velocity, shear rate and viscosity contours for a separating shear-thinning fluid. Here, $Re = 500$, $De = 3$, $n = 0.6$, $\alpha = 1$ and $\varepsilon = 0.15$. The overall effect of inertia on flow separation is inferred upon comparing the current flow to that in Figure 4 for $Re = 25$ (the remaining parameters are the same). These two flows are typical of the pre- and the post-critical ranges of Reynolds number. As will be discussed later, the critical Reynolds number at which the flow separates is strongly influenced by the viscosity parameters. A significant difference in streamline topology between Figures 7 and 4 is the appearance of a backflow region below the crest. There is also a significant loss of symmetry, particularly far from the lower wall. Although the dimensionless pressure is roughly 6 times larger than in the absence of separation, the difference between the actual pressures should be interpreted more carefully. In practice, for instance, if the increase in Reynolds number is due to the increase in velocity, then the actual pressure would increase significantly. However, if the increase in Re is due to a decrease in viscosity, the pressure would actually decrease. More importantly, it is clear that the (streamwise) pressure gradient has actually increased significantly. A large pressure gradient would force separation to occur, which is consistent with the present result.

The loss of symmetry with respect to $x = \lambda/2$ in the streamlines below the vortex is also reflected in the flow variables. Comparison with the $Re = 25$ flow (Figure 4) indicates that shearing has considerably increased near the lower wall. On the other hand, the maximum in v tends to be reduced, with its location shifted closer to the upper wall, for $Re = 500$ when compared to $Re = 25$. These changes can be attributed to the appearance of the wall vortex. The separation streamline reduces the effective cross-sectional flow area. Consequently, as a result of continuity, the streamwise velocity in the channel core remains high and the streamlines outside the recirculation are no longer parallel to the wall (i.e. these straighten out) and thus the maximum v is reduced when compared to the low-inertia case. Elongational effects (expansion and contraction) are thus weakened by inertia.

Other significant topological changes are observed just below the crest because of flow separation. Despite the apparent significance of the backflow, the magnitude of the velocity in the reverse direction is only 2% of the maximum in u (at the lower wall). The flow in the vertical direction weakens and loses symmetry. The pressure exhibits a minimum below the trough and a maximum below the crest, which are of the same magnitude (Figure 7). The

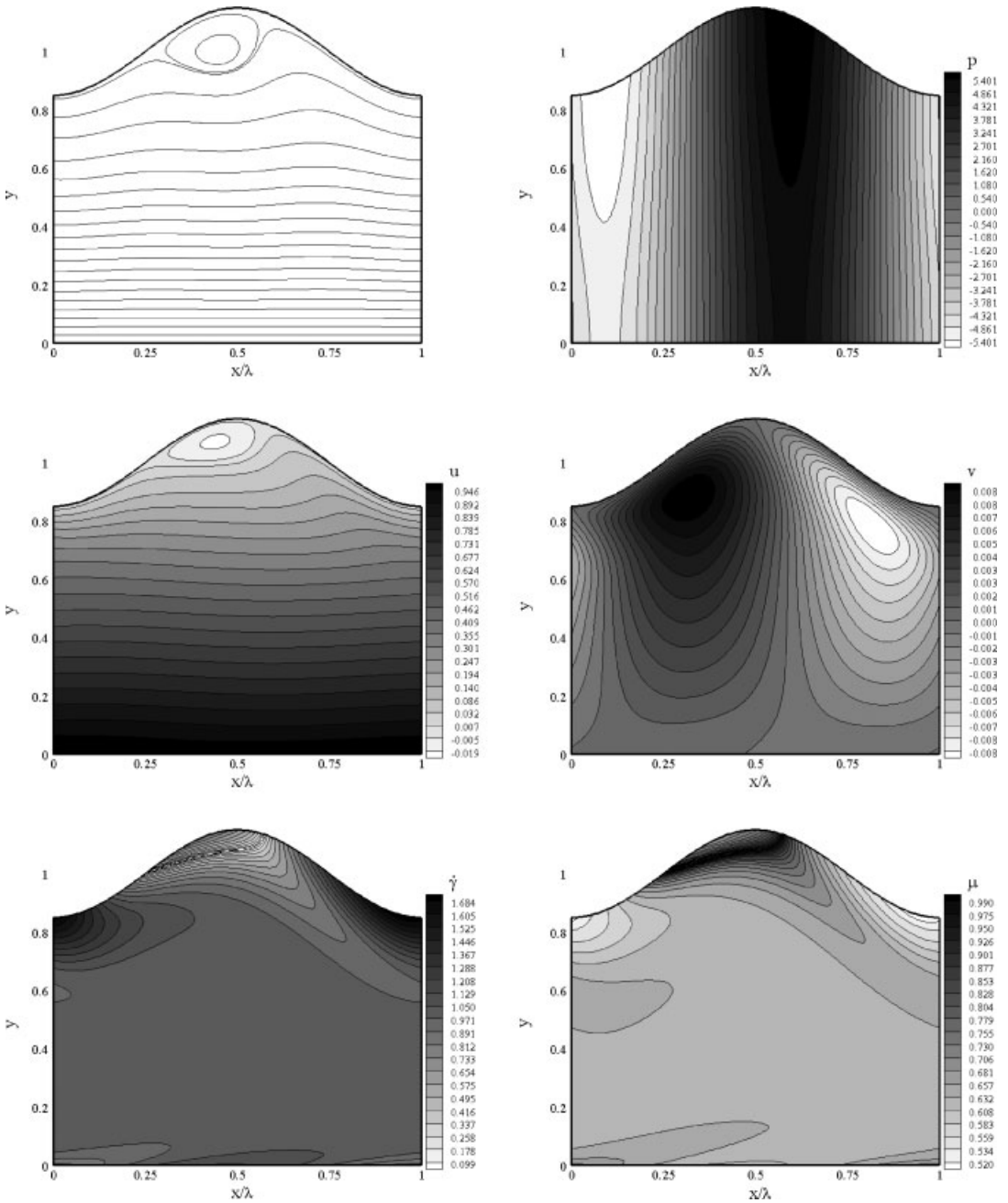

Figure 7. Typical response of a shear-thinning flow with high inertia ($Re = 500$). The figure displays the streamlines, the pressure, the contours of the streamwise and depthwise velocity components, shear rate magnitude, and viscosity. Here $\varepsilon = 0.15$, $\alpha = 1$, $n = 0.6$, $De = 3$ and $s = 0$.

regions of extrema extend further down (toward the lower wall) in the presence of separation. The pressure varies almost linearly with x between the two extrema. Significant distortion of the symmetry in shear rate (magnitude) and viscosity also results from separation. In particular, the regions of Newtonian behaviour are no longer located at the upper wall beneath the crest, and at the lower wall below the trough as indicated in Figure 4. For $Re = 500$, the Newtonian region is now off the upper wall, right in the core of the vortex. There are little Newtonian spots near the lower wall.

The effect of inertia is quantified further upon inspection of the normal and shear stresses. Their distributions are shown, respectively, in Figures 8 and 9 for $Re = 500$. The normal stress exhibits a sinusoidal dependence on x, which amplifies significantly with Re, shifting upstream, with no qualitative change (always sinusoidal dependence on x). The location of the extrema is independent of n for $Re = 500$ (see Figure 5 for comparison). Thus, for separating flow, the level of maximum normal stress, and not its location, can depend strongly on the type of fluid used. There does not seem to be any influence of inertia on the shear stress at the lower wall, despite the contraction resulting from separation. However, Figure 9 clearly indicates that the actual shear stress grows like Re. In contrast, the actual shear stress at the upper wall grows faster than Re. In particular, the shear stress maximum increases with Re, becoming positive for the small n range. Symmetry is lost about the crest, and a strong stress gradient develops near the point of reattachment. Thus, shear thinning tends to enhance separation, by effectively increasing inertia further.

3.3. *Influence of non-Newtonian effects on separation*

Whereas the influence of inertia on separation is well established, that of non-Newtonian effects is essentially unexplored. The onset of separation is now examined by varying n and De. The influence of the index n is typically illustrated in Figure 10. The figure shows the location of the points of separation and reattachment as function of the Reynolds number, for $n \in [0.2, 1.8]$, $De = 3$, $\varepsilon = 0.15$ and $\alpha = 1$. At a given Re, the separation point lies to the left, and the reattachment point lies to the right. The critical Reynolds number needed for the onset of vortex flow, Re_{cv}, is significantly dependent on n. In general, as Re increases above Re_{cv}, the size of the vortex increases until the vortex spans the entire period of the modulation. For shear-thickening fluids, the Re versus x/λ curve is typically narrow, exhibiting a strong minimum, from which Re_{cv} is readily identified. The vortex centre does not coincide with the midpoint of the wall period; it is located, as expected, slightly upstream of $x = \lambda/2$. Although the curves in the figure are dissymmetric with respect to $x = \lambda/2$, the separation and reattachment points remain symmetrically located with respect to the vortex centre. As n decreases, the curves tend to flatten, reflecting a weaker minimum. There is even a saturation effect of n in the low n range (the spacing between two successive curves decreases as n decreases). The saturation phenomenon is also encountered when other parameters are varied, such as ε, α and De (see below). Thus, for shear-thinning fluids, even a slight increase in Re above Re_{cv} leads to the onset of a relatively large vortex. More importantly, strongly shear-thinning fluids are likely to exhibit the onset of separation at any Reynolds number. This point will be further elaborated upon when separation in the absence of inertia is discussed (see later).

The value of the critical Reynolds number, Re_{cv} is probably the most important threshold parameter in the problem. This threshold is expected to be strongly influenced by the modu-

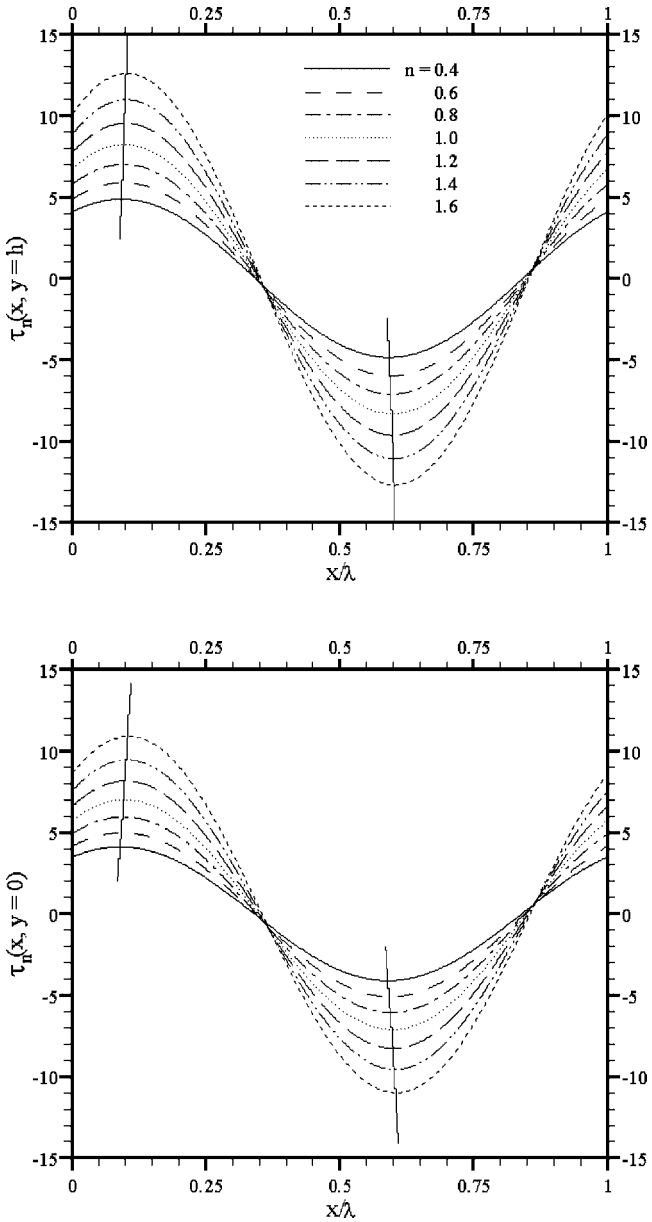

Figure 8. Influence of n (power law index) on the normal stress distribution at the upper (modulated) and lower (straight) walls for high inertia flow ($Re = 500$). Here $\varepsilon = 0.15$, $\alpha = 1$, $De = 3$ and $s = 0$.

lation amplitude, wavelength, and fluid parameters. Figures 11 and 12 show the influence of n on the dependence of Re_{cv}, and vortex location at onset, x_{cv}/λ, respectively, on the wall amplitude, ε, for $\alpha = 1$. Generally, Figure 11 indicates that Re_{cv} tends to decrease rapidly with ε, when ε is small, and eventually levels off as ε increases further. Non-Newtonian effects

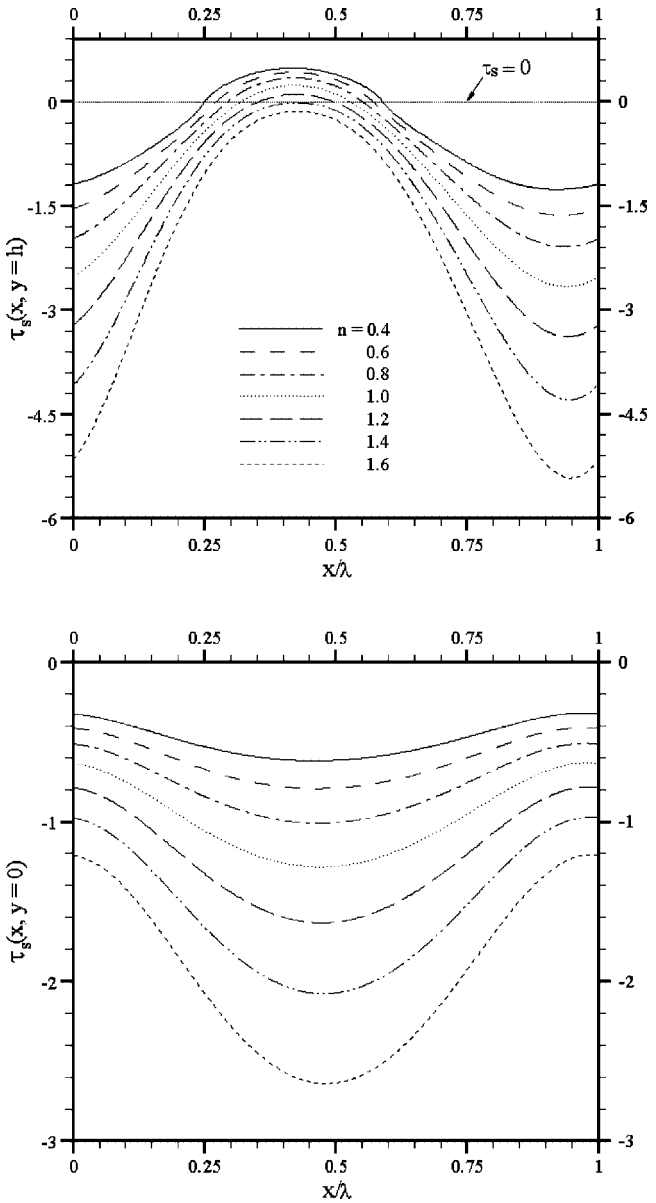

Figure 9. Influence of n (power law index) on the shear stress distribution at the upper (modulated) and lower (straight) walls for high inertia flow ($Re = 500$). Here $\varepsilon = 0.15$, $\alpha = 1$, $De = 3$ and $s = 0$.

appear to be much more significant for small amplitude modulation. For $\varepsilon > 0.25$, the critical Reynolds number is essentially independent of n and is very close to zero. These observations are expected to hold, at least qualitatively, when ε is increased further (at which point the current perturbation approach is no longer valid). Although the accuracy of the critical Re

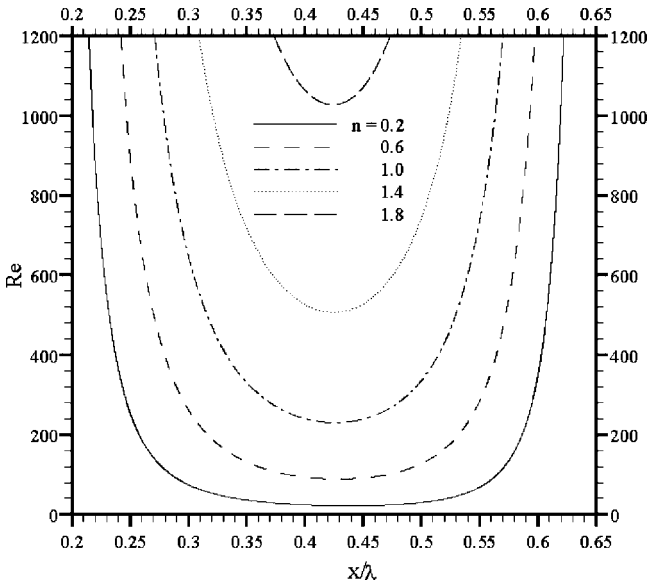

Figure 10. Influence of n on the locations of separation and reattachment points against the Reynolds number, for $De = 3$, $\alpha = 1$, and $\varepsilon = 0.15$.

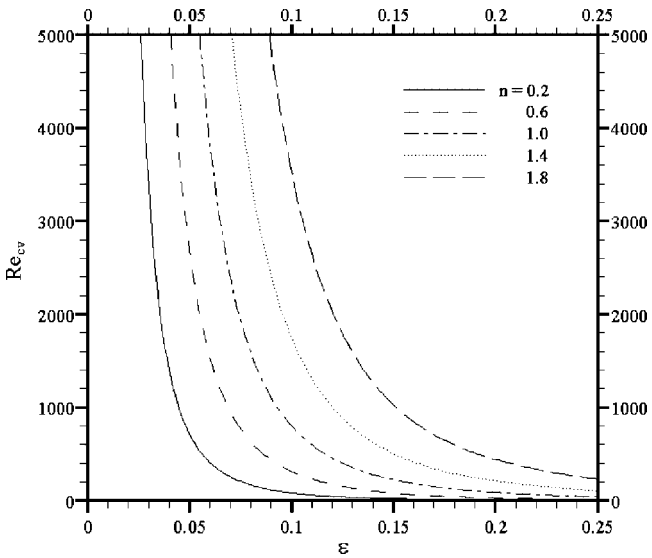

Figure 11. Influence of n on the critical Reynolds number, Re_{cv}, plotted against the modulation amplitude, ε, for $De = 3$ and $\alpha = 1$.

and the vortex location deteriorates as the wall amplitude increases, all the results reported in this study are within an acceptable accuracy ($< 5\%$). Thus, the results in Figure 12 should be interpreted along with those in Figure 3. Figure 12 indicates that the location of the separation

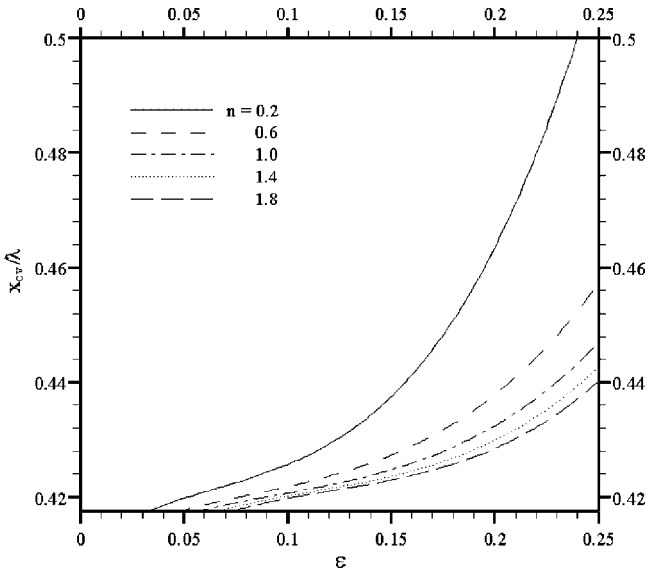

Figure 12. Influence of n on the location of the vortex centre, x_{cv}/λ, at onset, plotted against the modulation amplitude, ε, for $De = 3$ and $\alpha = 1$.

point at the onset tends to shift downstream as ε increases. A strong shift is predicted for small and large ε. At intermediate ε values there is essentially no change of the vortex centre location at onset. As n increases (from $n = 0.2$), the vortex centre tends to move upstream. However, there is a saturation in vortex position for moderately shear-thinning, Newtonian and shear-thickening fluids. It is interesting to observe from Figures 11 and 12 that while Re_{cv} remains practically uninfluenced by ε for large ε, x_{cv} grows sharply with ε. This means that the vortex centre eventually coincides with the geometrical centre of the modulation period. In other words, the vortex as well as the flow becomes symmetric. This is not surprising given the relative dominance of viscous effects (see also above).

Further insight on non-Newtonian effects is gained upon inspecting the influence of the time constant. Figures 13 and 14 show typically the influence of De on the location of the separation and reattachment points, for shear-thinning ($n = 0.6$) and shear-thickening ($n = 1.4$) fluids, respectively. Here, again, $\varepsilon = 0.15$ and $\alpha = 1$. As expected, the trends in the two cases are opposite. An increase in De tends to be destabilizing for a shear-thinning fluid, and stabilizing for a shear-thickening fluid. More importantly, there is a stronger saturation effect in the case of shear-thinning fluids than for shear-thickening fluids. The situation is further clarified from Figures 15 and 16, where Re_{cv} and x_{cv}/λ are plotted against n for $De \in [1, 18]$. Generally, the critical Reynolds number increases with n, almost exponentially. However, at small De, the increase is rather linear. Note that all the curves intersect at the Newtonian point. An almost opposite behaviour is depicted for x_{cv}.

It is important to observe that an explicit universal and functional relationship among Re_{cv}, ε and α exists for a Newtonian fluid, and may be written as

$$Re_{cv} = 0.77\varepsilon^{-3.01}\alpha^{-1.25} \tag{20}$$

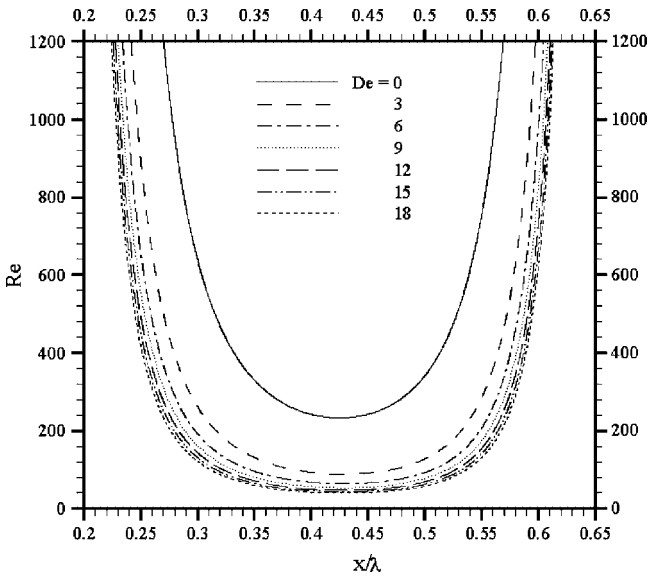

Figure 13. Influence of *De* on the locations of separation and reattachment points against the Reynolds number, for a shear thinning fluid $n = 0.6$, $\varepsilon = 0.15$, and $\alpha = 1.0$.

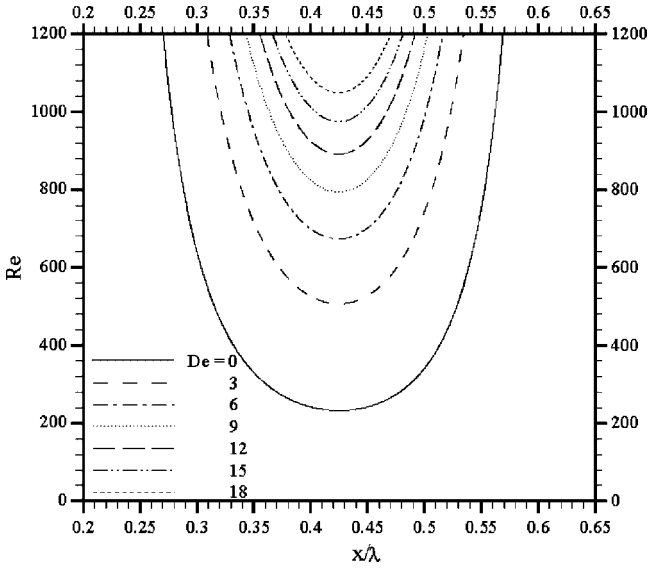

Figure 14. Influence of *De* on the locations of separation and reattachment points against the Reynolds number, for a shear thickening fluid $n = 1.4$, $\varepsilon = 0.15$, and $\alpha = 1.0$.

The fit is illustrated in Figure 17 where the symbols are based on formula (20). The location of the separation point will depend on streamline curvature, which depends on the local streamwise pressure gradient, which is a function of *Re* and ε, explicitly,

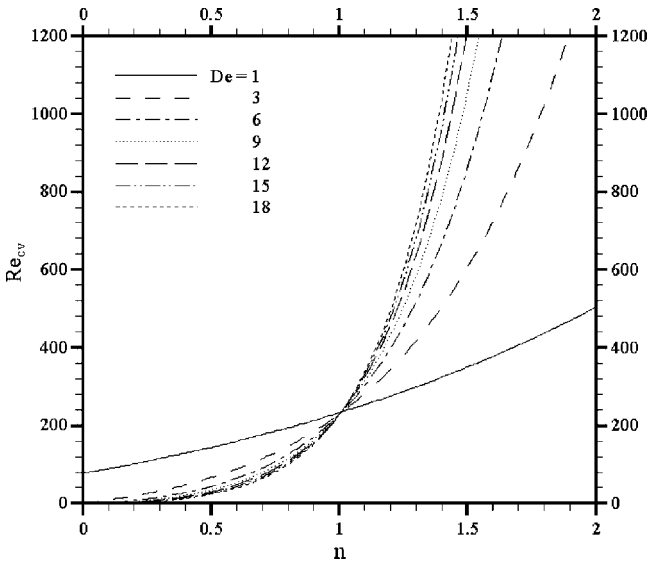

Figure 15. Influence of *De* on the critical Reynolds number, Re_{cv}, plotted against the power law index, n, for $\varepsilon = 0.15$ and $\alpha = 1.0$.

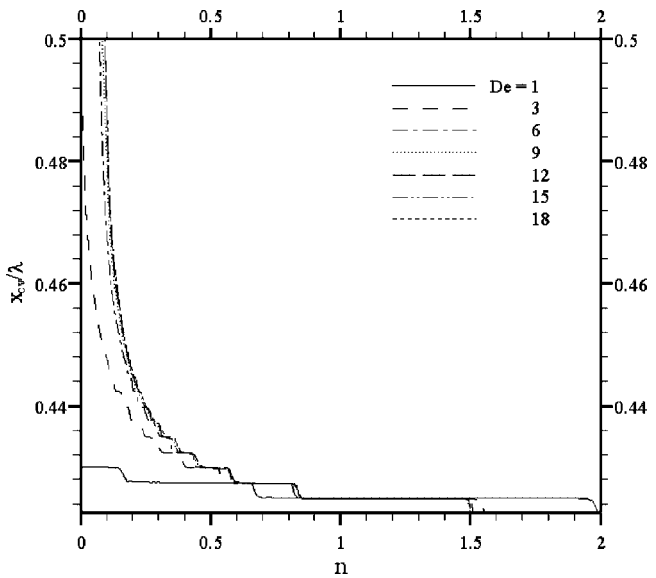

Figure 16. Influence of *De* on the location of vortex centre at onset, x_{cv}/λ, plotted against the power law index, n, for $\varepsilon = 0.15$ and $\alpha = 1.0$.

and implicitly on the streamline curvature, which can be characterized with the grouping $\varepsilon\alpha^2$.

Sobey [1] suggested the possible existence of such a relationship for pressure-driven flow. His results indicate a relationship of the type $\varepsilon^{-3}\alpha^{-1}$ for the sinusoidal modulation. However,

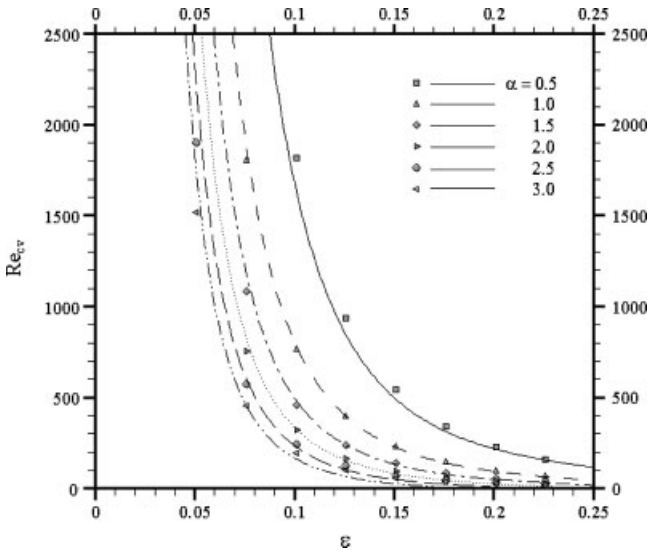

Figure 17. Influence of the wall modulation wavenumber on the critical Reynolds number, Re_{cv}, plotted against the modulation amplitude, ε, for Newtonian fluid, and $\alpha \in [0.5, 3.0]$. Symbols indicate the fit from Equation (20).

his parameter domain covered a very small range of α and ε, and the flow was symmetric with respect to the $y = 0$ axis. The relationship (20) is valid for the current flow configuration and over a larger domain of parameter values. Typically, Re_{cv} decreases dramatically with wall amplitude when ε is small. As ε increases further, the drop in Re_{cv} becomes less pronounced. In fact, there is an asymptotic decrease toward the zero limit. The drop is sharper and convergence (toward zero) is faster as α increases. A similar behaviour is observed when Re_{cv} is plotted against the modulation wavenumber. The overall influence of ε and α on the location of the vortex centre at onset is inferred from Figure 18. In contrast to the critical Reynolds number, there does not seem to be a universal behaviour that the vortex centre follows.

3.4. Separation at zero Reynolds number

The influence of non-Newtonian effects in the absence of inertia is an important issue, which will now be examined. Shear-thinning effects are expected to play a significant role in enhancing separation, as was discussed above (see Figure 10). In particular, it is found that separation would occur at practically any Reynolds number if shear-thinning effects were sufficiently strong. The question as to whether separation is possible at zero Reynolds number is a crucial one, which is now addressed. Upon setting $Re = 0$ in Equation (16), it is found that the flow can indeed separate if n is small and De is large. The response is typically illustrated in Figure 19 for $n = 0.05$, $De = 10$, $\varepsilon = 0.15$ and $\alpha = 1$. The figure shows the streamlines, the contours of velocity, pressure, shear rate and viscosity. The most striking feature in the figure, in comparison with Figure 7, is the absolute symmetry in the flow field. This may be surprising at first given that inertia-induced separation always causes the flow to lose symme-

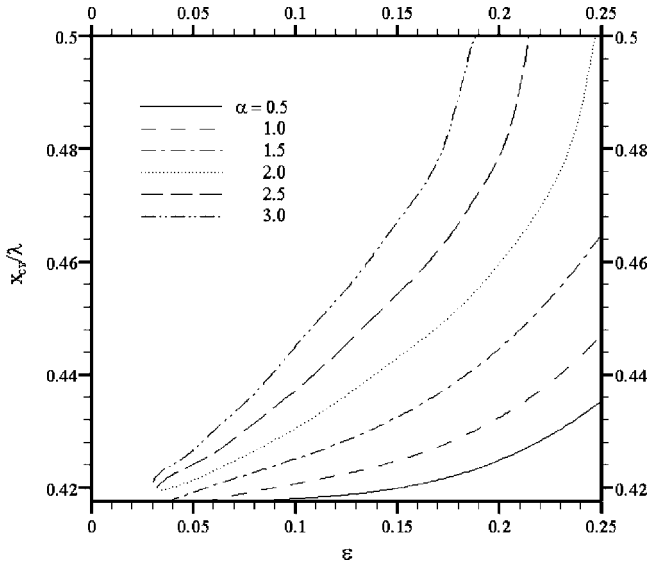

Figure 18. Influence of the wall modulation wavenumber on the location of the vortex centre at onset, x_{cv}/λ, plotted against the modulation amplitude, ε, for Newtonian fluid and $\alpha \in [0.5, 3.0]$.

try. In the absence of inertia, however, the symmetry breaking $x \to -x$ mechanism through the convective terms is no longer present. When $Re = 0$, full symmetry is predicted by the non-Newtonian equations, similar to creeping flow.

The pressure contours in Figure 19 reflect a weaker normal stress than earlier (see Figures 4 and 7). In the present case, the pressure maximum is more localized, essentially confined to the upper and lower walls (at $x/\lambda = 0.25$ and 0.75), instead of extending across the gap. The overall pressure and pressure gradient are significantly weaker as a result of dominance of shear thinning. The velocity and velocity gradients, as well as the shear rate, are essentially similar to low Reynolds-number flow (Figure 4). The viscosity distribution remains somewhat similar too, and its value is also unaltered despite the smaller n (0.05 compared to 0.6 in Figure 4); De is much larger in the present case (10 compared to 3).

3.5. *Numerical assessment*

The accuracy of the perturbation approach was addressed only partly in Section 3.1, where the lack of mass conservation was taken as a measure of relative error. Comparison with results based on the thin-film approximation was also conducted. The above assessment was necessary as it was possible to carry out for both Newtonian and non-Newtonian fluids. The issue regarding the absolute error is now addressed. Thus, the validation of the perturbation solution is further examined upon direct comparison with simulation results obtained using a finite-volume code, FLUENT. The assessment is introduced to the Newtonian flow first, and then to the shear thinning flow. Fluent includes special periodic boundary conditions that allow for the imposition of mass flow rate making the computation more straightforward when a specific flow Re is desired. Thus, for the present computations, periodic conditions were

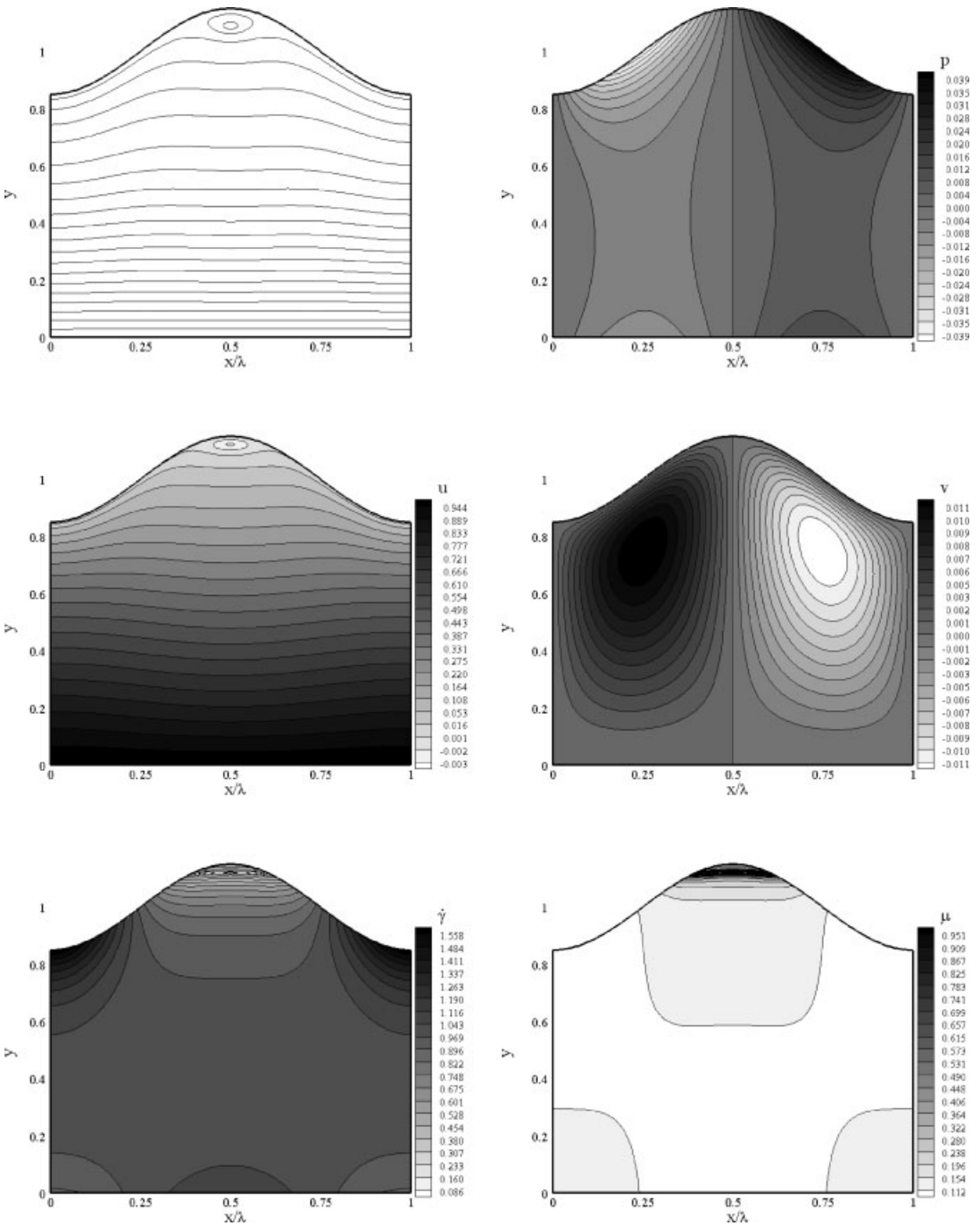

Figure 19. Typical response of a shear-thinning flow without inertia ($Re = 0$). The figure displays the streamlines, the pressure, the contours of the streamwise and depthwise velocity components, shear-rate magnitude, and viscosity. Here $\varepsilon = 0.15$, $\alpha = 1$, $n = 0.05$, $De = 10$ and $s = 0$.

imposed at the inlet and outlet, with the additional constraint of a mass flow rate. No-slip and zero-penetration conditions were imposed on the upper and lower walls. To ensure that the finite-volume predictions were independent of the mesh size, a grid-independence study was carried out for the case of $\alpha = 1$, $\varepsilon = 0.15$ and $Re = 1000$ for sinusoidal modulation. The grid density was progressively doubled until the results were grid-converged to within 1%; results presented in this study were computed on grids of 60×450 cells.

For comparison between the perturbation and finite-volume methods, the average mass flow rate obtained from the perturbation solution is used in the CFD code to generate the flow. Simultaneously, a linear pressure gradient is also generated by the code, which is compared against the zero imposed (linear) pressure gradient used for the perturbation method. The finite-volume method generated a very small pressure gradient, almost zero, which is in good agreement with the perturbation method-imposed pressure gradient. Furthermore, the two methods generate similar pressure contours at various conditions. One can conclude, thus, the high accuracy of the perturbation method pressure distribution presented in Figures 4, 7, and 19.

The mean flow patterns obtained using the two methods are very similar. Quantitatively, the more sensitive parameters are the critical Reynolds number for separation, the location of the separation and reattachment points. Earlier studies on pressure-driven Newtonian flow through modulated channels indicated that differences in the prediction of the separation point between finite-volume and perturbation methods differ by less than 1% and are thus of order ε^2. However, differences in the predictions of the reattachment point are much larger, of the order of 5% (order ε), and increase as Re increases [34, 38]. However, a better quantitative assessment is obtained by comparing the streamwise velocity profiles based on the finite-volume and perturbation simulations at a given location. This comparison is shown in Figure 20 at two locations for $Re = 1000$, $\alpha = 1$ and $\varepsilon = 0.15$. The locations, $x = \lambda/2$ (Figure 20a) and $x = \lambda$ (Figure 20b), coincide, respectively, with a crest and a trough, where the relative error is greatest. The figure shows the y-distribution of the total streamwise velocity component, u, and the perturbation contribution u^1. The perturbation component differs from the finite-volume simulation results by an order ε. The overall solution is consequently accurate to within ε^2. It is noteworthy that the trend in u^1 is correctly predicted at all points and the error is in the magnitude. Moreover, the locations of the separation and reattachment points appear to be reasonably well predicted. For further detail on the accuracy of the present approach for a Newtonian fluid, the reader is referred to the paper by Zhou *et al.* [34].

Since this work is devoted to explain non-Newtonian effects, assessing the accuracy of the perturbation approach for non-Newtonian fluids is necessary. The perturbation approach accuracy does not seem to be affected by the presence of non-Newtonian parameters as inferred from Figure 21. This figure shows the y-distribution of the total streamwise velocity component, u, and the perturbation contribution u^1 based on the finite-volume and perturbation simulations at $x = \lambda/2$ (Figure 21a) and $x = \lambda$ (Figure 21b) for $De = 3$, $n = 0.6$, $Re = 1000$, $\alpha = 1$ and $\varepsilon = 0.15$. The perturbation component differs from the finite-volume simulation results by an order ε. The overall solution is consequently accurate to within ε^2. It is noteworthy that the trend in u^1 is correctly predicted at all points and the error is in the magnitude.

The question regarding the validity of the perturbation approach in describing the non-linear phenomenon of vortex formation is critical. Strictly speaking, the perturbation approach is not valid at the locations where shear stress vanishes, separation and reattachment points, since both the leading- and higher-order terms in the shear stress become of the same order of magnitude. It seems, however, that the error generated is only of *local* and not *global* nature.

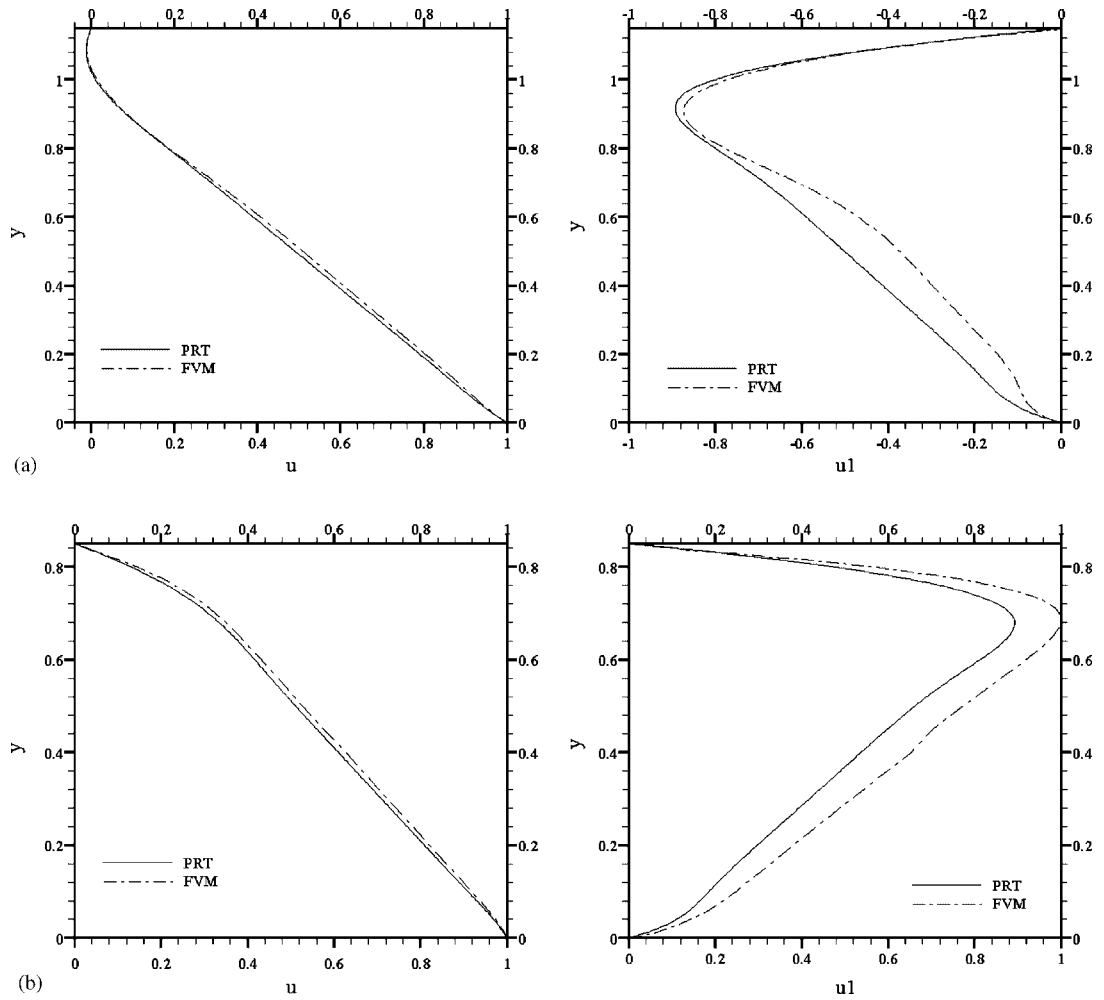

Figure 20. Comparison between finite-volume and perturbation methods. Streamwise velocity distribution: (a) below the crest at $x = \lambda/2$; and (b) below the trough at $x = \lambda$, for $Re = 1000$, $\varepsilon = 0.15$ and $\alpha = 1$. The figure shows the distributions based on the perturbation (solid) and finite-volume (dash-dot) methods.

In fact, the error generated at the separation and reattachment points does not influence the accuracy elsewhere. This claim is substantiated by the extensive comparison and agreement between the fully non-linear and the linearized solutions. Even the locations of the separation and reattachment points, and therefore the vortex size, appear to be accurately predicted by the perturbation approach (see, for instance, [34, Table 1]). The accuracy is secured in this case, at least in part, because of the close proximity of the vortices to the stationary wall, which ensures that the higher-order velocity terms must be small since both the leading term and the overall velocity are themselves small.

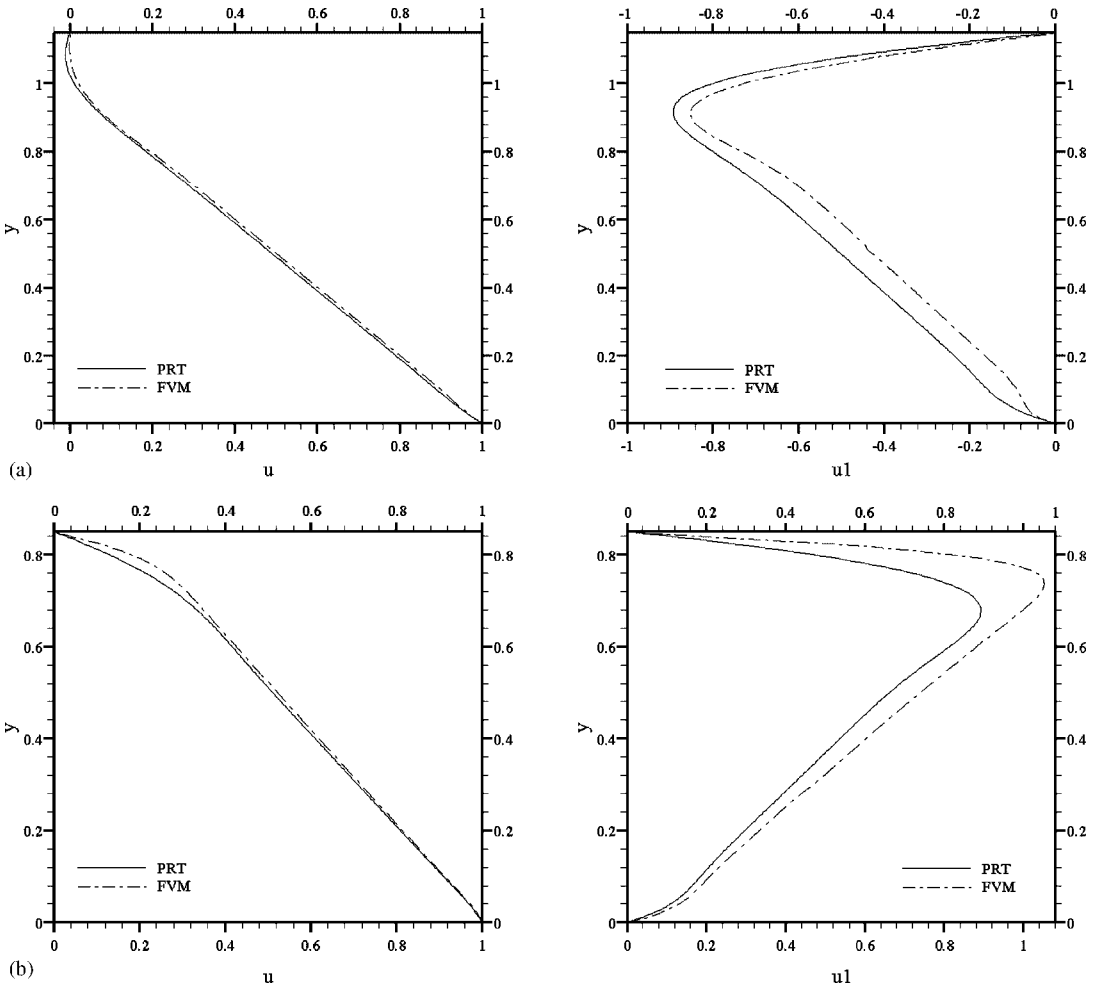

Figure 21. Comparison between finite-volume and perturbation methods. Streamwise velocity distribution: (a) below the crest at $x = \lambda/2$; and (b) below the trough at $x = \lambda$, for $De = 3$, $n = 0.6$, $Re = 1000$, $\varepsilon = 0.15$ and $\alpha = 1$. The figure shows the distributions based on the perturbation (solid) and finite-volume (dash-dot) methods.

4. CONCLUDING REMARKS

The interplay between inertial and non-Newtonian effects is examined in this study, for the flow in weakly modulated channels. A perturbation approach is applied to obtain the flow field and stresses. A comparative assessment is carried out against results based on a two-dimensional finite-volume code for Newtonian flow. The range of validity of the method is also assessed on the basis of conservation of mass. The main advantage of the perturbation solution is its ease in implementation, and the essentially negligible CPU and storage requirements, compared to a full finite-volume simulation. The influence of inertia, non-Newtonian

parameters, modulation amplitude and wavelength is emphasized. In particular, the effect of these parameters and their influence on conditions of flow separation, onset of vortex flow, vortex size and location is systematically examined. Non-Newtonian effects are found to have drastic influence. Shear thinning can lead to separation in the absence of inertia.

ACKNOWLEDGEMENTS

This work was supported by the Natural Sciences and Engineering Research Council of Canada.

REFERENCES

1. Sobey IJ. On flow through furrowed channels, Part 1: calculated flow patterns. *Journal of Fluid Mechanics* 1980; **96**:1–26.
2. Pilitsis S, Beris AN. Calculation of steady-state viscoelastic flow in an undulating tube. *Journal of Non-Newtonian Fluid Mechanics* 1989; **31**:231–287.
3. Stephanoff KD, Sobey IJ, Bellhouse BJ. On flow through furrowed channels, Part 2: observed flow patterns. *Journal of Fluid Mechanics* 1980; **96**:27–32.
4. Nishimura T, Ohoriand Y, Kawamura Y. Flow characteristics in a channel with symmetric wavy wall for steady flow. *Journal of Chemical Engineering of Japan* 1984; **17**:466–471.
5. Nishimura T, Murakami S, Arakawa S, Kawamura Y. Flow observations and mass transfer characteristics in symmetrical wavy-walled channels at moderate Reynolds numbers for steady flow. *International Journal of Heat and Mass Transfer* 1990; **33**:835–845.
6. Tanda G, Vittori C. Fluid flow and heat transfer in a two-dimensional wavy channel. *Heat and Mass Transfer* 1996; **31**:411–418.
7. Sleath JFA. A numerical study of the influence of bottom roughness on mass transport by water waves. *Proceedings of the International Conference on Numerical Methods in Fluid Dynamics*, Southampton, U.K., 1973.
8. Vajravelu K. Fluid flow and heat transfer in horizontal wavy channels. *Acta Mechanica* 1980; **35**:245–258.
9. Benjamin B. Shearing flow over a wavy boundary. *Journal of Fluid Mechanics* 1959; **6**:161.
10. Dyke MV. *Perturbation Methods in Fluid Mechanics*. Academic Press: New York, London, 1964.
11. Selvarajan S, Tulapurkara EG, Vasanta Ram V. Stability characteristics of wavy walled channel flows. *Physics of Fluids* 1999; **11**:579–589.
12. Tsangaris S, Leiter E. On laminar steady flow in sinusoidal channels. *Journal of Engineering Mathematics* 1984; **18**:89–103.
13. Selvarajan S, Tulapurkara EG, Vasanta Ram V. A numerical study of flow through wavy-walled channels. *International Journal for Numerical Methods in Fluids* 1998; **26**:519–531.
14. Thompson JF, Warsi ZUA, Wayne Mastin C. *Numerical Grid Generation, Foundations and Applications*. North-Holland: New York, 1985.
15. Caponi EA, Fornberg B, Knight DD, McLean JW, Saffman PG, Yuen HC. Calculations of laminar viscous flow over a moving wave surface. *Journal of Fluid Mechanics* 1982; **124**:347–362.
16. Nayfeh AH. *Introduction to Perturbation Techniques*. Wiley: New York, 1981.
17. Nayfeh AH. *Problems in Perturbation*. Wiley: New York, 1985.
18. Shivamoggi BK. *Perturbation Methods for Differential Equations*. Birkhäuser: Boston, 2003.
19. Deane AE, Keverkidis IG, Karniakadis GE, Orszag SA. Low-dimensional models for complex flows: application to grooved channels and circular cylinders. *Physics of Fluids A, Fluid Dynamics* 1991; **3**:2337–2354.
20. Szumbarski J, Floryan JM. A direct spectral method for determination of flows over corrugated boundaries. *Journal of Computational Physics* 1999; **153**:378–402.
21. Wang G, Vanka SP. Convective heat transfer in periodic wavy passages. *International Journal of Heat and Mass Transfer* 1995; **38**:3219–3230.
22. Guzman AM, Amon CH. Flow patterns and forced convective heat transfer in converging–diverging channels. *ASME HTD* 1993; **237**:43–53.
23. Guzman AM, Amon CH. Transition to chaos in converging–diverging channel flows: Ruelle-Takens-Newhouse scenario. *Physics of Fluids* 1994; **6**:1994–2002.
24. Blancher S, Creff R, Batina J, Andre P. Hydrodynamic stability in periodic geometry. *Finite Elements in Analysis and Design* 1994; **16**:261–270.
25. Ahrens M, Yoo YJ, Joseph DD. Hyperbolicity and change of type in the flow of viscoelastic fluids through pipes. *Journal of Non-Newtonian Fluid Mechanics* 1987; **24**:67–83.

26. Marshall RJ, Metzner AB. Flow of viscoelastic fluids through porous media. *Industrial and Engineering Chemistry Fundamentals* 1967; **6**:393–403.
27. Beris AN, Avgousti M, Souvaliotis A. Spectral calculation of viscoelastic flows: evaluation of Giesekus constitutive equation in model flow problems. *Journal of Non-Newtonian Fluid Mechanics* 1992; **44**: 197–228.
28. Giesekus H. A simple constitutive equation for polymer fluids based on the concept of the deformation-dependent tensorial mobility. *Journal of Non-Newtonian Fluid Mechanics* 1982; **11**:69–109.
29. Pilitsis S, Beris AN. Viscoelastic flow in an undulating tube. Part II. Effects of high elasticity, large amplitude of undulation and inertia. *Journal of Non-Newtonian Fluid Mechanics* 1991; **39**:375–405.
30. Davidson DL, Graessley WW, Schowalter WR. Velocity stress fields of polymeric liquids in a periodically constricted channel, Part 1. Experimental methods and straight channel validations. *Journal of Non-Newtonian Fluid Mechanics* 1993; **49**:317–344.
31. Davidson DL, Graessley WW, Schowalter WR. Velocity stress fields of polymeric liquids in a periodically constricted channel, Part 2. Observation of non-Newtonian behavior. *Journal of Non-Newtonian Fluid Mechanics* 1993; **49**:345–375.
32. Pilitsis S, Souvaliotis A, Beris AN. Viscoelastic flow in a periodically constricted tube: the combined effect of inertia, shear thinning and elasticity. *Journal of Rheology* 1991; **35**:605–646.
33. Ashrafi N, Khayat RE. A low-dimensional approach to nonlinear plane-Couette flow of viscoelastic fluids. *Physics of Fluids* 2000; **12**:345–365.
34. Zhou H, Khayat RE, Martinuzzi RJ, Straatman AG. On the validity of the perturbation approach for the flow inside weakly modulated channels. *International Journal for Numerical Methods in Fluids* 2002; **39**:1139–1159.
35. Bird RB, Armstrong RC, Hassager O. *Dynamics of Polymeric Liquids*, vol. 1. Wiley: New York, 1987.
36. Garg VK, Maji PK. Laminar flow and heat transfer in a periodically converging–diverging channel. *International Journal for Numerical Methods in Fluids* 1988; **8**:579–597.
37. Pereyra V. PASVA3: an adaptive finite-difference FORTRAN program for first order nonlinear boundary value problems. *Lecture Notes in Computer Science*. Springer: Berlin, 1978; **76**:67–88.
38. Zhou H, Martinuzzi RJ, Khayat RE, Straatman AG, Abu-Ramadan E. Influence of wall shape on vortex formation in modulated channel flow. *Physics of Fluids* 2003; **15**:3114–3133.

